CHAPTER SIXTEEN

First-Principles Calculations of Electronic and Optical Properties of $LiAlH_4$ in its Monoclinic and Tetragonal Phases

S. Djeroud and F. Adjailia
Physics Laboratory at Guelma, Department of Material Sciences, Faculty of Mathematics, Informatics and Material Sciences, University 8 Mai 1945 Guelma, P.O. Box 401, Guelma 24000, Algeria

Contents

Abstract

In this paper we present first-principles calculations for the electronic and optical properties for the complex hydride $LiAlH_4$ employing the full-potential linearized plane wave plus local orbitals (FP-LAPW s+ lo) method. The exchange and correlation potential is a generalized gradient approximation.

The band structures, total and partial density of states, and dielectric functions are calculated at equilibrium in the monoclinic and tetragonal phases. For the monoclinic phase, present results agree well with the previous theoretical data. They also show that the tetragonal phase has a direct band gap of 4.11 eV and its DOS is similar to that at the transition pressure. In the optical spectra, absorption increases rapidly to intense peaks. Their origin is identified from the band structures. The refractive index $n(\omega)$, reflectivity $R(\omega)$, absorption coefficient $I(\omega)$, and energy-loss function $L(\omega)$ are calculated and discussed for the both phases.

Advances in Quantum Chemistry, Volume 68
ISSN 0065-3276, http://dx.doi.org/10.1016/B978-0-12-800536-1.00016-2

1. INTRODUCTION

The sharp increase of carbon dioxide in the atmosphere is caused by the use of carbon fossil fuels (coal, natural gas, oil) in transport, habitat, and industry. This disturbing phenomenon has led the scientific community to find an alternative source of clean and renewable energy which can be consumed without any significant negative impact on the environment. Several solutions have been proposed such as solar, wind, and hydrogen. This last solution seems promising and hydrogen is expected to play an important role in a future energy economy, especially in the transport sector,[1,2] reducing emission of greenhouse gas and pollutants.[3,4] Hydrogen is one of the most abundant elements on the planet. Hydrogen is present in water; it is not available in nature. The major challenge is therefore to extract it and to store it suitably in dense and safe media in order to distribute then. Hydrogen stored in solid materials is a safe alternative to liquid or compressed gas. In this context, research activities were focused on seeking compounds that can store hydrogen. Many advanced materials such as complex hydrides have been explored.[5–7] Ternary hydrides of light elements have attracted much attention for their low weight and high hydrogen content.[8] Since the work of Bogdanovic and Schwickardi in 1997,[9] $NaAlH_4$ and $LiAlH_4$ have drawn great interest as candidates for reversible storage. Absorption kinetics are improved by adding catalysts (Ti, V).[9,10]

Extensive experiments and theoretical studies have been performed to determine the structural stability,[11–13] the nature of chemical bond,[14] and understanding electronic and thermodynamic properties of these compounds.[15–19] Concerning their optical properties, there is still a lack of data.

In this work we focused into the optical properties of the ternary aluminum hydride $LiAlH_4$. In ambient conditions $LiAlH_4$ crystallizes as monoclinic α-$LiAlH_4$.[12] With increasing pressure, the phase transition from α- to β-$LiAlH_4$ occurs at 2.6 GPa.[13,17] Above 33.86 GPa the β phase is converted into γ-$LiAlH_4$.[20] The monoclinic structure of $LiAlH_4$ with space group P21/c has four formula units per crystallographic cell. AlH_4 forms an almost regular tetrahedral subunit with an Al atom at its center and four H atoms at its vertices. Li atoms separate these subunits of the composed structure. The tetragonal structure β-$LiAlH_4$ has I41/a symmetry. The crystallographic cell contains two formula units. The crystal structure can also be described in terms of AlH_4 tetrahedra. The orthorhombic structure γ-$LiAlH_4$ with space group Pnma has four formula units per crystal cell. In this case an octahedral environment is formed around the metal Al.

There is a considerable work on the monoclinic phase of $LiAlH_4$[8,14–16,19,21,22] but very few results are available on its two phases β and γ.[16] On the other hand the dielectric function was studied in the α phase.[22] To the best of our knowledge, there are no calculations of optical properties that have been reported for the tetragonal and orthorhombic phases of $LiAlH_4$. To determine how the optical properties depend on structure, we report here first-principles studies of the electronic properties, absorptive and dispersive parts of the dielectric function, and other optical properties in the ambient and high-pressure phases of $LiAlH_4$.

The rest of this paper is organized as follows: in Section 2, we describe the method used and we give the details of calculations. The results on structural, electronic and optical properties are presented and discussed in Section 3. Finally, a brief conclusion is found in Section 4.

2. COMPUTATIONAL DETAILS

The calculated results in this paper were obtained using the full-potential linearized augmented plane wave plus local orbitals (FP-LAPW + lo)[23,24] method within the framework of density functional theory (DFT)[25,26] as implemented in the WIEN2k code.[27] This method uses "the muffin-tin geometry", separating space into spheres and interstices. For the exchange correlation potential we used the generalized gradient approximation as defined by Perdew et al.[28]

In this paper the core states that are completely confined inside the corresponding muffin-tin spheres were treated fully relativistically, while for the valence states we used the scalar-relativistic approach (all the relativistic effects are taken into account except the spin-orbit coupling).

In the calculations, the H ($1s^1$), Li ($1s^2 2s^1$), and Al ($2p^6 3s^2 2p^1$) states are treated as valence electrons. The muffin-tin radii R_{MT} are chosen such that the MT spheres do not overlap. They are taken to be 0.9 Bohr for H and 2 Bohr for Li and Al for the phases α-, and β-$LiAlH_4$. For γ-$LiAlH_4$, R_{MT} corresponds to 1.09 Bohr for H, 2.37 Bohr for Li and 2.02 Bohr for Al. The basis functions were expanded up to $R_{MT} \times K_{MAX} = 5$ for α-, and γ-$LiAlH_4$, and 5.5 for β-$LiAlH_4$ (where R_{MT} is the smallest of all MT spheres radius and K_{MAX} is the maximum value of the wave vector K).

The number of k-points, which ensures total energy convergence in the whole Brillouin zone, was 48 for the monoclinic, 130 for the tetragonal,

and 85 k-points for the orthorhombic $LiAlH_4$ structures. The self-consistent calculations are considered to be converged when the total energy is stable within 0.1 mRyd.

3. RESULTS AND DISCUSSION

3.1 Structural properties

The proposed crystal structures of the investigated compound $LiAlH_4$ were optimized. We have proceeded as follows: first, experimental and theoretical values available in the literature were used for optimizing the total energy as a function of cell volume, keeping c/a and b/a constant and the internal atomic coordinates were fully relaxed at each value of cell volume. We note that the parameter β in the monoclinic structure was kept fixed at the reported experimental value. The self-consistent calculations are considered to be converged when the force is less than 0.3 mRyd/Bohr.

Figure 16.1 displays the optimized structures which clearly show the AlH subunits. The total energy-volume curves $E(V)$ were fitted to the Murnaghan equation of state (EOS).[29] The obtained results are illustrated in Figure 16.2.

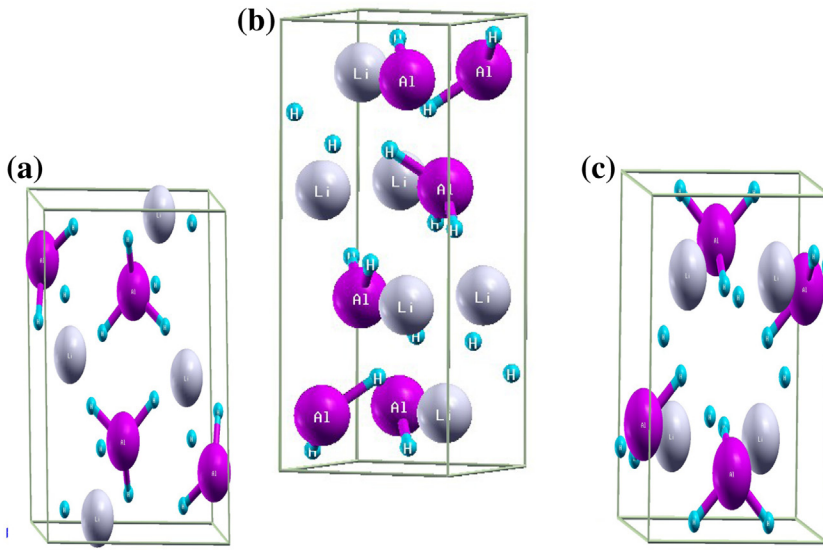

Figure 16.1 Crystal structure of $LiAlH_4$ with the optimized lattice parameters and the relaxed atomic positions: (a) monoclinic: P21/c, (b) tetragonal: I41/a, and (c) orthorhombic: Pnma. The small spheres are H, the large dark spheres are Al, and the large light spheres are Li. For color version of this figure, the reader is referred to the online version of this chapter.

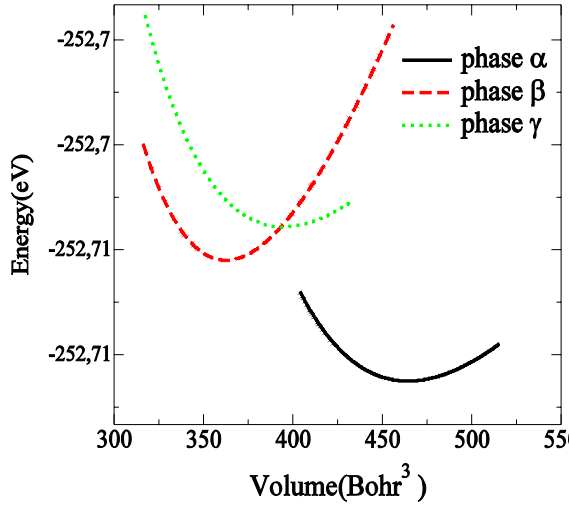

Figure 16.2 The total energy-volume curves of the structures α-, β-, and γ-$LiAlH_4$. For color version of this figure, the reader is referred to the online version of this chapter.

The lattice parameters and internal atomic positions identified at the equilibrium for α-, β-, and γ-$LiAlH_4$ are listed in Table 16.1, together with the available experimental data and previous theoretical woks for comparison. It is observed from Table 16.1 that for the phase α-$LiAlH_4$, the optimized parameters are consistent with the experimental values[12] with a slight increase of 0.3%. Compared to the previous theoretical works of Vajeeston et al.[16] who used the projected augmented plane wave (APW) as implemented in Vienna ab initio simulation package (VASP)[30] within the generalized gradient approximation GGA, the calculated lattice parameters show a slight underestimation of 2% in the tetragonal structure and an increase of 0.8% in the orthorhombic structure of $LiAlH_4$. Overall, our results are in good agreement with the available data.

As it is shown in Figure 16.2, the total energy for α-$LiAlH_4$ is the smallest which confirms the greater stability of the monoclinic structure than the tetragonal and orthorhombic ones.

The calculated equilibrium volume V_0 per formula unit, bulk modulus B_0 and its corresponding pressure derivative B_0' are summarized in Table 16.2 for all phases of $LiAlH_4$.

As we can observe in Table 16.2, our calculated B_0 and B_0' agree well with experimental data reported by Talysin et al.[31] and Chellappa et al.,[32] so with results reported in Ref. 16.

We note that the bulk modulus of β-$LiAlH_4$ is larger than those of α and γ phases but its equilibrium volume is the smallest. This can lead to an increase in hydrogen storage capacity as the investigated compound $LiAlH_4$

Table 16.1 Optimized structural parameters for α-, β-, and γ-$LiAlH_4$ with experimental data and other calculations

Structure	Lattice constants (Å)		Atom coordinates	
	This work	Other	This work	Other
α-$LiAlH_4$ (P21/c)	$a = 4.8355$	(4.8174)[a]	Li: .5769, .4620, .8272	(.5603, .4656, .8266)[a]
	$b = 7.8314$	(7.8020)[a]	Al: .1529, .2042, .9347	(.1386, .2033, .9302)[a]
	$c = 7.8509$	(7.8214)[a]	H1: .1936, .1009, .7660	(.1826, .0958, .7630)[a]
	$\beta = (112.228)$[a]		H_2: .3685, .3749, .9807	(.3524, .3713, .9749)[a]
			H_3: .2468, .0840, .1165	(.2425, .0806, .1148)[a]
			H_4: .8083, .2654, .8730	(.7994, .2649, .8724)[a]
β-$LiAlH_4$ (I41/a)	$a = 4.5659$	(4.6611)[b]	Li: 0, .25, .625	(0, .25, .625)[b]
	$c = 10.3071$	(10.5219)[b]	Al: 0, .25, .125	(0, .25, .125)[b]
			H: .2479, .5781, .5408	(.2527, .4237, 5413)[b]
γ-$LiAlH_4$ (Pnma)	$a = 6.5196$	(6.4667)[b]	Li: .2465, .25, .2474	(.2428, .25, .2467)[b]
	$b = 5.3916$	(5.3478)[b]	H_1: .2984, .25, .9591	(.3067, .25, .9617)[b]
	$c = 6.6471$	(6.5931)[b]	H_2: .7 147, .25, .9614	(.7162, .25, .9631)[b]
			H_3: .4934, .0208, .2947	(.4889, .9833, .2943)[b]

[a]From Ref. 12. [b]From Ref. 16.

Table 16.2 Equilibrium volume V_0 ($Bohr^3$/f.u.), Bulk modulus B_0 (GPa) and its corresponding pressure derivative B_0' for α-, β-, and γ-$LiAlH_4$ with other calculations and experimental data

	This work			Other	
Structure	V_0	B_0	B_0'	B_0	B_0'
α-$LiAlH_4$	68.80	13.90	5.64	12.9[c]	4.1
β-$LiAlH_4$	53.72	25.07	4.89	25.64[d]	4.35
γ-$LiAlH_4$	58.50	14.26	5.40	14.25[b]	4.85

[b]From Ref. 16. [c]From Ref. 31. [d]From Ref. 32.

has high weight content of hydrogen. Hence, we explore the possibility of stabilizing the β phase at ambient pressure.[16] The properties of β-$LiAlH_4$ under normal conditions are sought.

In our following analysis, we are interested in the electronic and optical properties of both α and β phases. The phase γ-$LiAlH_4$ is much less stable and will be investigated in the future.

3.2 Electronic properties

By using the structural parameters determined at equilibrium, we have calculated the electronic structures of $LiAlH_4$ for the phases α-, and β-$LiAlH_4$. The calculated band structures are displayed in Figure 16.3 along some higher symmetry directions of their Brillouin zone. The Fermi level is taken as the origin of energies.

Note in Figure 16.3, for the monoclinic phase α-$LiAlH_4$ the valence band maximum is located at the Γ point and the conduction band minimum is located at the C point which causes an indirect band gap of about 4.89 eV. While, the second phase β-$LiAlH_4$ shows a direct band gap at the Γ point at about 4.11 eV.

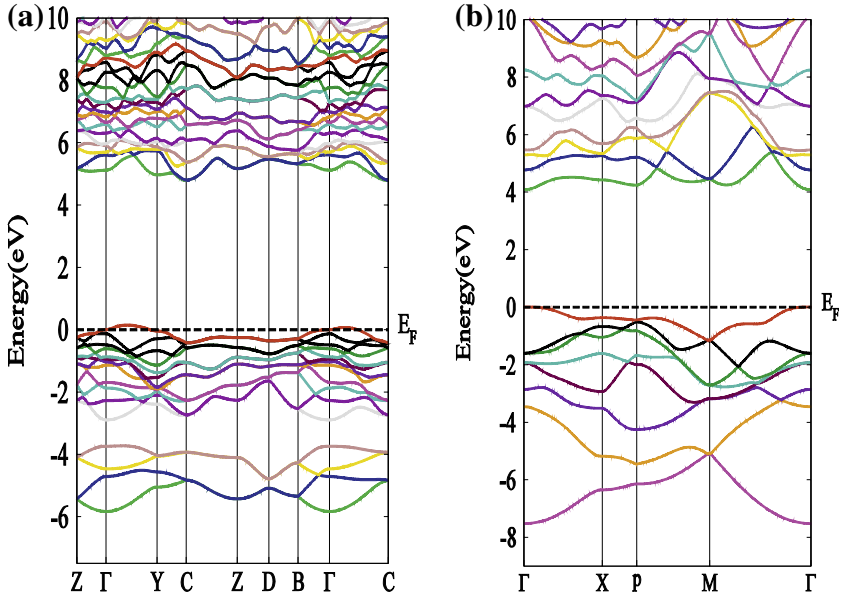

Figure 16.3 Band structures for (a) α-$LiAlH_4$ and (b) β-$LiAlH_4$. For color version of this figure, the reader is referred to the online version of this chapter.

Table 16.3 The calculated energy gap E_g (eV) of $LiAlH_4$ in the monoclinic and tetragonal structures at the equilibrium volume, with other calculations

	E_g (eV)	
Structure	**Present work**	**Other calculations**
α-$LiAlH_4$	4.89	4.71[b], 4.8[e], 4.77[f], 4.19[f], 6.6[f]
β-$LiAlH_4$	4.11	4.25[b]

[b] From Ref. 16. [e] From Ref. 19. [f] From Ref. 22.

It is interesting to compare our calculated band gaps with other results. In Table 16.3 we have compared our work and other results. From the band gap values listed in Table 16.3, the GGA calculations on α-$LiAlH_4$, by Vajeeston et al.[16] Orgaz et al.,[19] and Setten et al.,[22] agree well with our value. The band gap obtained by the LDA approximation[22] is ∼0.7 eV less and that which GW calculations give[22] is higher. The band gap shown in β-$LiAlH_4$ is in good agreement with that in Ref. 16.

We have also calculated the total and partial density of states (DOS) corresponding to the band structures plotted in Figure 16.3. The calculated DOS are illustrated in Figures 16.4 and 16.5 for α-, and β-$LiAlH_4$, respectively. As shown in Figure 16.4 the valence band is divided into two regions separated by a small gap of ∼0.9 eV. Its lowest energy state is dominated by Al-s states, while the higher one, close to the Fermi level is due to H-s and Al-p states with small contribution of Al-d, Li-s and Li-p states.

From α- to β-$LiAlH_4$ the small gap disappears from Figure 16.5. The DOS curves displayed in Figure 16.5 show that the valence band is contributed by H-s states and more mixing of Al-s and Al-p states with a minority of Al-d, Li-s and Li-p states. In both the phases the conduction band has very much less H character. Our results are consistent with those reported in Ref. 16. Note that the most significant finding in electronic properties for β-$LiAlH_4$ is that the calculated density of states at equilibrium is similar to that obtained at transition pressure: $P = 2.6$ GPa.

3.3. Optical properties

The optical properties of crystals are essentially determined by the complex dielectric function $\varepsilon(\omega) = \varepsilon_1(\omega) + i\ \varepsilon_2(\omega)$, which characterizes the linear response of the material to an electromagnetic radiation. The

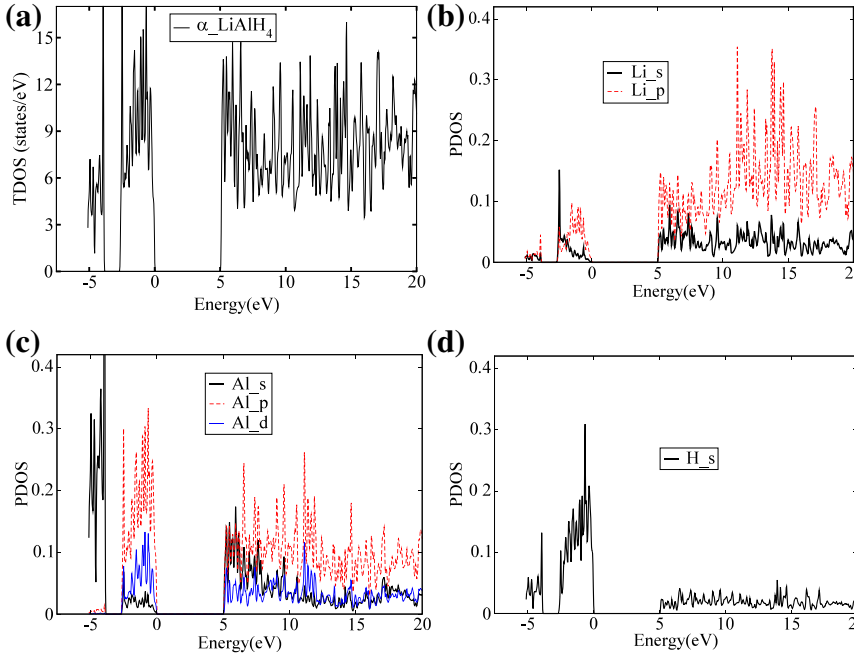

Figure 16.4 Total and partial density of states for α-$LiAlH_4$: (a) TDOS and (b), (c) and (d) PDOS. For color version of this figure, the reader is referred to the online version of this chapter.

imaginary part $\varepsilon_2(\omega)$ of the dielectric function represents the optical absorption in the crystal. The interband contribution to the imaginary part of $\varepsilon(\omega)$ is calculated by summing transitions from occupied to unoccupied states over the Brillouin zone; taking the appropriate momentum matrix elements into account, the imaginary part is given by the following expression:[33]

$$\mathrm{Im}\,\varepsilon(\omega)=\varepsilon_2(\omega)=\frac{4\pi^2e^2}{m^2\omega^2}\sum_{i,j}\int|\langle i|M|j\rangle|^2\left(f_i\left(1-f_j\right)\right)\delta\left(E_f-E_i-h\omega\right)d^3k \tag{1}$$

where $\hbar\omega$ is the energy of the incident photon, e and m the electron charge and mass, M the momentum operator, $|i\rangle$ is the wave function with eigenvalue E_i, and f_j the Fermi distribution for $|i\rangle$ state.

The Kramers–Kronig expression gives the real part $\varepsilon_1(\omega)$ of the dielectric function from the imaginary:

$$\varepsilon_1(\omega)=1+\frac{2}{\pi}\int_0^\infty\frac{\varepsilon_2\left(\omega'\right)\omega' d\omega'}{\omega'^2-\omega^2} \tag{2}$$

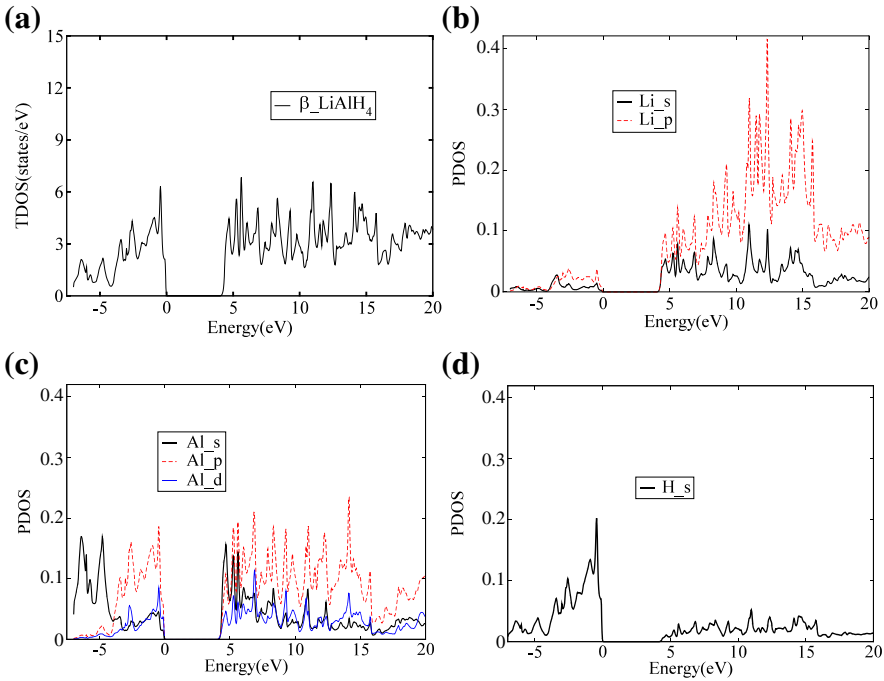

Figure 16.5 Total and partial density of states for β-$LiAlH_4$: (a) TDOS and (b), (c) and (d) PDOS. For color version of this figure, the reader is referred to the online version of this chapter.

For the calculations of optical spectra, a sufficiently dense k-mesh is used, which consists of $(25 \times 14 \times 15)$ and $(18 \times 18 \times 18)$ k-meshes for α-, and β-$LiAlH_4$, respectively.

The imaginary and real parts of the dielectric function were calculated for both phases α-, and β-$LiAlH_4$ whose band structures are given in Figure 16.3. Our results are shown in Figures 16.6 and 16.7 for radiation to 25 eV.

Due to the monoclinic symmetry the dielectric function is resolved in three components for α-$LiAlH_4$. These components of the electric field direction perpendicular and parallel to the crystallographic z-axis are labeled ε_{xx}, ε_{yy}, and ε_{zz}. With tetragonal symmetry the dielectric tensor may have two components ε_{xx} (ε_{yy}) and ε_{zz} also corresponding to the electric field direction perpendicular and parallel to the crystallographic z-axis.

The $\varepsilon_2(\omega)$ curves shown in Figure 16.6 for α-$LiAlH_4$ are characterized by one major absorption peak along each Cartesian axis. What attracts attention in this structure is the presence of a shoulder in the z-direction in the region of lower energy and for photon energy higher than those corresponding to the mean peaks, $\varepsilon_2(\omega)$ exhibits three shoulders, one

along the *y*-axis and the others along the *x*-axis. For β-$LiAlH_4$ it is clear from Figure 16.6 that each component has one absorption peak. ε_{2zz} is the highest and is shifted toward lower energy. There is an intense shoulder at 5.13 eV in the *x*-direction. Above the energy of the maximum dielectric absorption, $\varepsilon_2(\omega)$ decreases.

Slight anisotropy is observed between the components of $\varepsilon_2(\omega)$ for α-$LiAlH_4$, especially in the region of the principle peaks. However for the phase β, the absorptive components are clearly separated from each other, in particular in the region of intense absorption. The shape of the $\varepsilon_2(\omega)$ curves is remarkably similar to that obtained in Ref. 22 where Setten et al. have carried out a recent study on the directionally averaged dielectric function of $LiAlH_4$ in GW (Green function, W shielded Coulomb term) work. We see slight tail at lower energy for β-$LiAlH_4$.

For analyzing the structures of the calculated imaginary part $\varepsilon_2(\omega)$, we have used the technique of decomposition of the optical spectra, technique employed in studies on cubic semiconductor,[34] filled tetrahedral semiconductors,[35] and orthorhombic compounds.[36] The results of decomposing each spectrum to its individual pair contribution, i.e., the contribution from each pair of valence vi and conduction cj bands (not shown here), indicate that

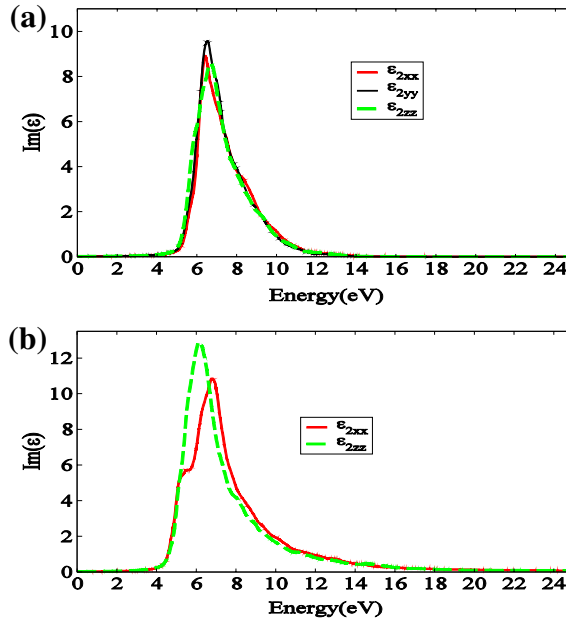

Figure 16.6 Imaginary part of the dielectric function for (a) α-$LiAlH_4$ and (b) β-$LiAlH_4$. For color version of this figure, the reader is referred to the online version of this chapter.

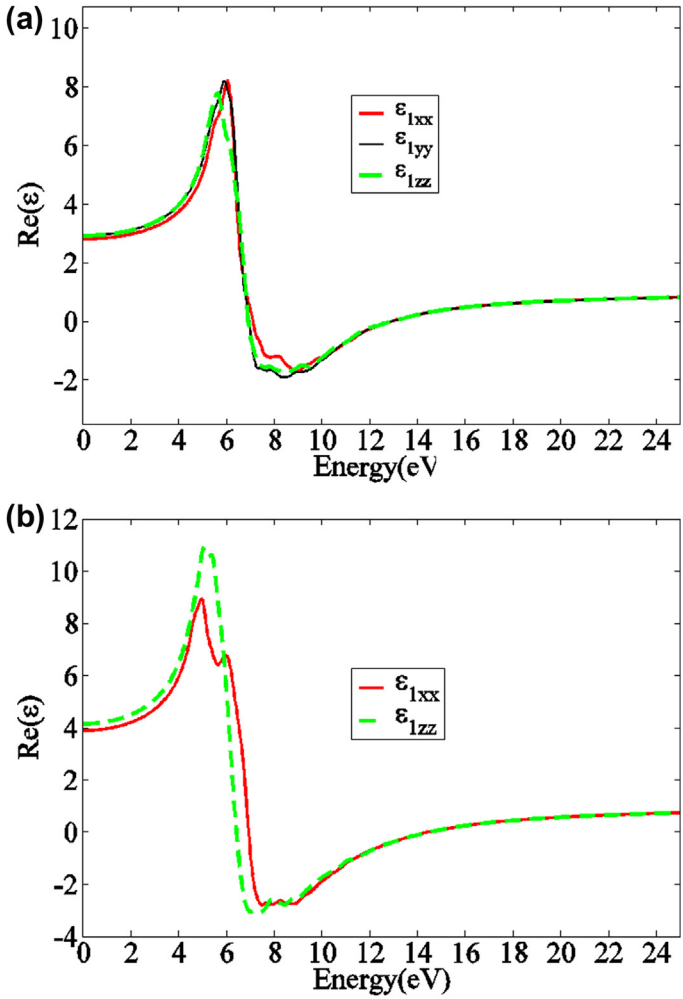

Figure 16.7 Real part of the dielectric function for (a) α-$LiAlH_4$ and (b) β-$LiAlH_4$. For color version of this figure, the reader is referred to the online version of this chapter.

the first absorption starts at energies 5.1 and 4.11 eV for α-, and β-$LiAlH_4$, respectively. This comes from direct transitions from the higher valence band to the conduction band just above the Γ point.

For α-$LiAlH_4$ the threshold is slightly higher than the calculated indirect band gap (4.89 eV).

As shown in Figure 16.6 the absorptive part of the dielectric function increases rapidly above the threshold. The major peak occurring at 6.40 eV, along *x*-axis, originates from the following transitions:

(i) $v_3 \rightarrow c_4$ (6.38 eV) at the Z point,
(ii) $v_5 \rightarrow c_{1,2}$ (6.35 eV) at the D point,
(iii) $v_6 \rightarrow c_2$ (6.53 eV) at the Γ and D points,
(iv) $v_7 \rightarrow c_1$ (6.26 eV) and $v_7 \rightarrow c_1$ (6.38 eV) at the Z and B points, respectively.

(Numbering of bands is from the upper valence band and the lower conduction band).

At lower energy two shoulders appear along the *x*-axis. The first one starts at energy 8.17 eV and it is due to a series of weak transitions from the higher valence to the higher conduction bands. For the second shoulder happening at around 9.37 eV, the lowest valence bands play their role.

The major transitions which contribute to the principal peak reached at 6.51 eV, along **y**-axis, are as follows:

(i) $v_1 \rightarrow c_6$ (6.30 eV), $v_2 \rightarrow c_6$ (6.49 eV), $v_3 \rightarrow c_5$ (6.45 eV), $v_5 \rightarrow c_2$ (6.45 eV), $v_6 \rightarrow c_2$ (6.55 eV) at the Γ point,
(ii) $v_2 \rightarrow c_5$ (6.41 eV) at the C point,
(iii) $v_4 \rightarrow c_4$ (6.35 eV) at the Z point,
(iv) $v_6 \rightarrow c_1$ (6.45 eV) and $v_7 \rightarrow c_2$ (6.60 eV) at the D point,
(v) $v_7 \rightarrow c_1$ (6.42 eV) at the B point.

Just after the highest absorption, the shoulder observed in region 6.76–7.32 eV is essentially due to the transitions $v_1 \rightarrow c_{10}$, $v_2 \rightarrow c_8$, and $v_{2,3,4} \rightarrow c_7$.

The major peak located at 6.65 eV, along ***z***-axis, originates from the following transitions:

(i) $v_1 \rightarrow c_8$ (6.79 eV) in the region (C–Z) and $v_1 \rightarrow c_8$ (6.94 eV) at the Z point,
(ii) $v_1 \rightarrow c_9$ (6.86 eV) and $v_7 \rightarrow c_2$ (6.67 eV) at the Γ point,
(iii) $v_3 \rightarrow c_5$ (6.48 eV) at the C point,
(iv) $v_1 \rightarrow c_7$ (6.52 eV), $v_5 \rightarrow c_2$ (6.36 eV), $v_5 \rightarrow c_1$ (6.36 eV), $v_6 \rightarrow c_4$ (6.57 eV), $v_7 \rightarrow c_1$ (6.54 eV) at the D point.

The shoulder at 6.05 eV arises from the transitions from the first four valence bands to the conduction bands.

For **β-$LiAlH_4$** the dielectric absorption starts above the threshold corresponding to the calculated direct band gap. The shoulder observed in region 5.13–5.75 eV, along ***x***-axis, originates at its beginning from the direct transitions $v_1 \rightarrow c_{1,2}$ with the energy transition (5.15 eV) in the region (P–M) in Brillouin zone.

The major contributions at the end of this shoulder are essentially the transitions:

(i) $v_1 \rightarrow c_2$ (5.59 eV) at the X and P points,
(ii) $v_2 \rightarrow c_1$ (5.67 eV) at the Γ point,
(iii) $v_2 \rightarrow c_2$ (5.61 eV) at the M point,
(iv) $v_3 \rightarrow c_2$ (5.63 eV) in the region (X–P).

After this shoulder, $\varepsilon_2(\omega)$ increases rapidly and the main peak reached at 6.78 eV stems from the following transitions:

(i) $v_1 \rightarrow c_5$ (6.79 eV) near P, $v_2 \rightarrow c_4$ (6.98 eV) and $v_3 \rightarrow c_3$ (6.83 eV) at the Γ point,
(ii) $v_2 \rightarrow c_3$ (6.80 eV) and $v_5 \rightarrow c_1$ (6.20 eV) at the P point,
(iii) $v_3 \rightarrow c_4$ (6.71 eV) at the X point.

The major peak along z-axis occurs at around 6.13 eV and originates from the transitions:

(i) $v_3 \rightarrow c_2$ (6.13 eV) in the region (Γ–X),
(ii) $v_2 \rightarrow c_1$(6.26 eV) at the Γ point,
(iii) $v_2 \rightarrow c_2$ (5.96 eV) and $v_4 \rightarrow c_3$ (6.98 eV) at the X point,
(iv) $v_2 \rightarrow c_3$ (6.35 eV) and $v_3 \rightarrow c_3$ (6.62 eV) at the P point.

From this analysis we can conclude that, for the ambient α-$LiAlH_4$, the responsible transitions of the principal peaks occur from the valence bands situated in the region close to the Fermi level E_F. The real parts $\varepsilon_1(\omega)$ of the dielectric function are displayed in Figure 16.7 for α-, and β-$LiAlH_4$ on Cartesian axes.

Figure 16.7 shows that starting at the values $\varepsilon_1(0)$, the real part increases with increasing photon energy, reaches major peaks, and becomes zero. After passing through a minimum the dispersive part $\varepsilon_1(\omega)$ reaches the zero again at about 12.4 and 14.4 eV for α-, and β-$LiAlH_4$. N.B. here $\varepsilon_2(\omega)$ plotted in Figure 16.6 is very small. The static dielectric constant $\varepsilon_1(0)$ from the zero frequency limit of $\varepsilon_1(\omega)$ was calculated and is listed in Table 16.4 for both phases.

We now consider the other frequency-dependent linear optical constants such as the refractive index $n(\omega)$, the reflectivity $R(\omega)$, the absorption coefficient $I(\omega)$, and the energy-loss function $L(\omega)$ from the dielectric function using relations in Ref. 37. The refractive index which describes the behavior of an electromagnetic wave in a medium was calculated. The spectra are displayed in Figure 16.8 where we can observe that the refractive index generally follows the shape of the real part at which it is related by $n(0) = \sqrt{\varepsilon_1(0)}$. The calculated static refractive index $n(0)$ and the energy corresponding to $n = 1$ are summarized in the same table together with $\varepsilon_1(0)$.

Note from Table 16.4 that the β-$LiAlH_4$ with its smaller band gap than α-$LiAlH_4$ has the highest values of the static dielectric constant and static refractive index. To our knowledge no experimental or theoretical data are available for comparison. Also the calculated results show that the real part $\varepsilon_1(\omega)$ and the refractive index $n(\omega)$ are anisotropic. This is slight for the components for α-$LiAlH_4$. A pronounced anisotropy is observed for β-$LiAlH_4$.

Another optical interesting constant that we consider in this study is the reflectivity. The results of this optical parameter are shown in Figure 16.9.

Analysis of calculated spectra shows that the reflectivity starts at very small values ~6% for α-$LiAlH_4$, grows at different rates along the x-, y-, and z-axes. The energy range 6.5–12.3 eV has characteristic peaks. A major one of about 68% at 11.71 eV is on the y-axis. For β-$LiAlH_4$, starting at 10% and 11% for x-, and z-axes, the reflectivity spectra show a larger region characterized by strong reflectivity. The maximum of about 70% is located at 13.4 eV. At higher energy the reflectivity decreases rapidly. Anisotropy is pronounced for the both phases.

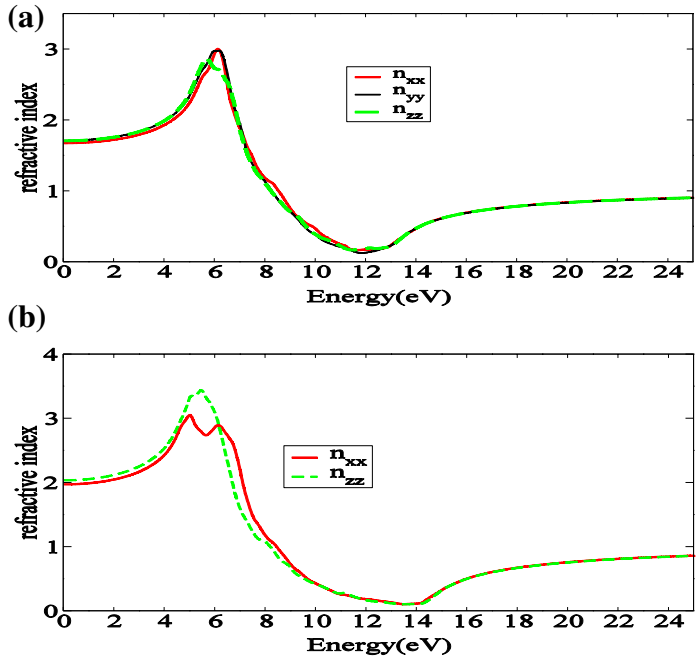

Figure 16.8 Refractive index $n(\omega)$ for (a) α-$LiAlH_4$ and (b) β-$LiAlH_4$. For color version of this figure, the reader is referred to the online version of this chapter.

Table 16.4 Calculated static dielectric constant and static refractive index with the energy corresponding to $n=1$, for α- and β-$LiAlH_4$ along *x*-, *y*-, and *z*-directions

Structure	$\varepsilon_1(0)$			$n(0)$			E_{eV} $(n=1)$		
	xx	*yy*	*zz*	*xx*	*yy*	*zz*	*xx*	*yy*	*zz*
α-$LiAlH_4$	2.8179	2.9384	2.9278	1.6785	1.7141	1.7111	8.5035	8.3214	8.2042
β-$LiAlH_4$	3.9055	3.9055	4.1606	1.9762	1.9762	8.4219	2.0397	2.0397	8.1770

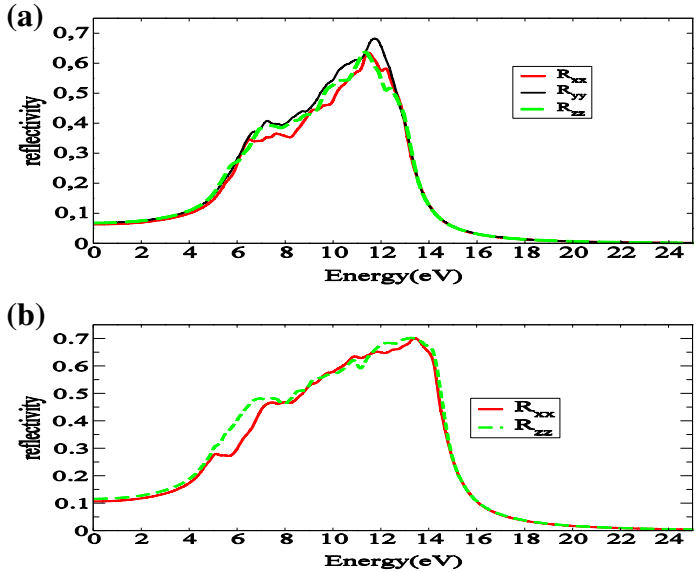

Figure 16.9 Reflectivity $R(\omega)$ for (a) α-$LiAlH_4$ and (b) β-$LiAlH_4$. For color version of this figure, the reader is referred to the online version of this chapter.

Figure 16.10 shows the absorption coefficient for α-, and β-$LiAlH_4$. The absorption coefficient $I(\omega)$ is larger ($10^4\,cm^{-1}$) and increases rapidly. For α-$LiAlH_4$ the strong peak is observed at 7.19 eV along *y*-axis. The absorption spectra indicate maximums in the energy range 7.19–8.80 eV.

For β-$LiAlH_4$, I_{zz} is highest and occurs at 6.73 eV with the major peak along *x*-axis at 7.22 eV. Since the band structures of β-$LiAlH_4$ have more dispersion than for α-$LiAlH_4$, absorption of β-$LiAlH_4$ has a wide energy range.

The energy-loss function $L(\omega)$ is an important factor describing the energy loss of the fast electrons crossing in the material. The energy-loss function can be evaluated from the dielectric function. It can be described by the expression

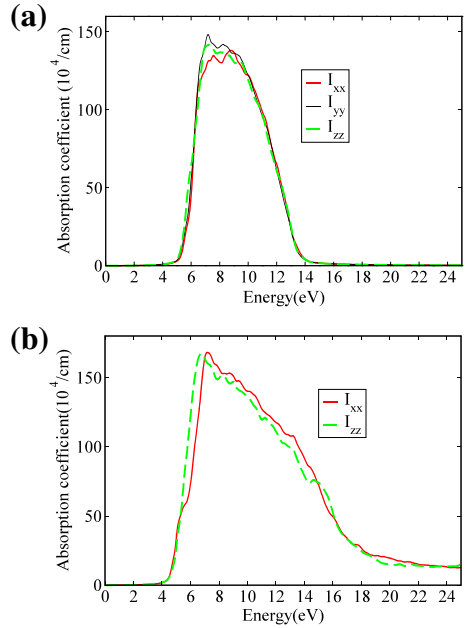

Figure 16.10 Absorption coefficient $I(\omega)$ for (a) α-$LiAlH_4$ and (b) β-$LiAlH_4$. For color version of this figure, the reader is referred to the online version of this chapter.

$$L(\omega) = \mathrm{Im}\left(-\frac{1}{\varepsilon(\omega)}\right) \tag{3}$$

which can be also written as:

$$L(\omega) = \frac{\varepsilon_2(\omega)}{\varepsilon_1(\omega)^2 + \varepsilon_2(\omega)^2} \tag{4}$$

Our obtained results are plotted in Figure 16.11.

As shown in Figure 16.11 the energy-loss spectra show significant values in the energy region situated between 11.7 and 13.7 eV for α-$LiAlH_4$. The intense peak is observed at energy 12.96 eV along the all Cartesian axes. Concerning β-$LiAlH_4$, its energy range 13.5–15 eV is characterized by much energy loss. The major peaks are located at around energy 14.4 eV. The peak along the z-axis is the highest. Note that for both α-, and β-$LiAlH_4$ the major peak occurs when $\varepsilon_2(\omega)$ is very small and $\varepsilon_1(\omega)$ reaches the zero again. The mean peak in the energy-loss function is the plasma frequency ω_p. Therefore the $\hbar\omega_p$ plasmon energy from its peak position is 12.96 and 14.4 eV for α-, and β-$LiAlH_4$.

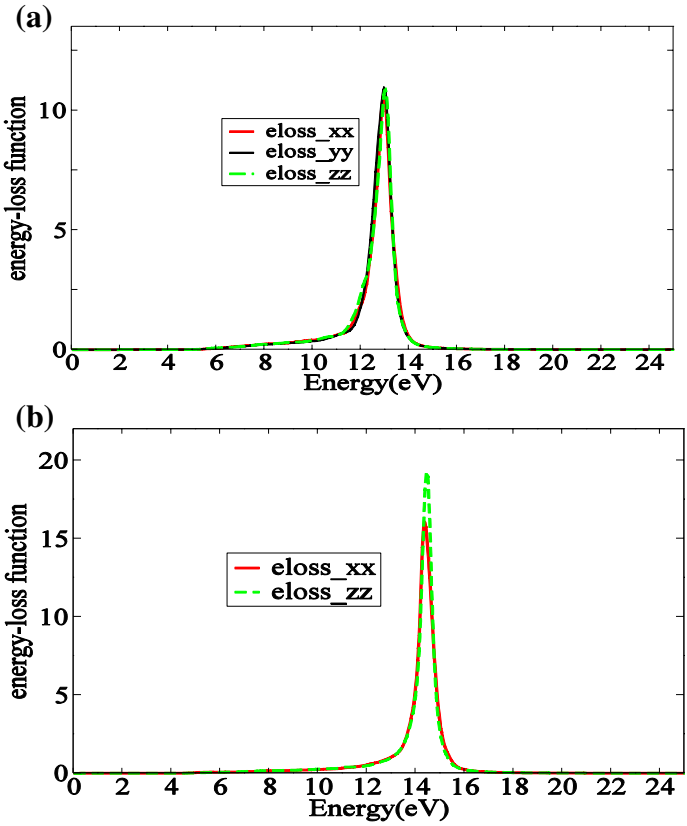

Figure 16.11 Energy-loss function for (a) α-$LiAlH_4$ and (b) β-$LiAlH_4$. For color version of this figure, the reader is referred to the online version of this chapter.

4. CONCLUSION

The present calculations use the full-potential linearized augmented plane wave plus local orbitals (FP-LAPW + lo) method with the generalized gradient approximation (GGA).

The structural properties are calculated for various phases for $LiAlH_4$. The energy minimization indicates that α is stablest. Comparison of the equilibrium volume of these structures shows that β has the lower equilibrium volume.

The band structures, total and partial density of states are investigated at equilibrium for α-, and β-$LiAlH_4$. Our calculations show that the results for α-$LiAlH_4$ agree well with the previous theoretical data. They also show

that β-$LiAlH_4$ has a direct band gap of 4.11 eV and its DOS is similar to that at the transition pressure $P = 2.6$ GPa.

The dielectric functions are calculated and presented in this paper. The optical absorption increases rapidly and the intense peak is at 6.51 eV along y-axis and at 6.13 eV along z-axis for α-, and β-$LiAlH_4$, respectively. The absorption for β-$LiAlH_4$ covers a larger energy range. Based on the band structures we have ascribed the peaks in the imaginary part and found that transitions occurred between the highest valence bands and the lowest conduction bands are responsible for most of the optical absorption. Higher photon energy involves bands near the Fermi level.

The frequency-dependent linear optical constants such as the refractive index $n(\omega)$, reflectivity $R(\omega)$, absorption coefficient $I(\omega)$, and energy-loss function $L(\omega)$ are calculated and discussed in this paper for the both phases.

ACKNOWLEDGMENT

The authors acknowledge Dr. Kamel Zanat for computational support.

REFERENCES

1. Schlapbach, L.; Z ttel, A. Hydrogen-Storage Materials of Mobile Application. *Nature* **2001**, *414*, 3538.
2. Dresselhaus, M. S.; Thomas, I. L. Alternative Energy Technologies. *Nature* **2001**, *414*, 3327.
3. Thomas, J. M.; Raja, R. Hydrogen Storage for Energy Application. *Annu. Rev. Mater. Res.* **2005**, *35*, 315.
4. Schultz, M. G.; Dielh, T.; Brasseur, G. P.; Zittel, W. Air Pollution and Climate-Forcing Impacts of a Global Hydrogen Economy. *Science* **2003**, *302* (5645), 624–627.
5. Vajeeston, P.; Ravindran, P.; Kjekshus, A.; Fjellvag, H. High Hydrogen Content Complex Hydrides: A Density-Functional Study. *Appl. Phys. Lett.* **2006**, *89*, 071906.
6. Kang, Jeung Ku; Kim, Se Yun; Han, Young Soo; Muller, Richard P.; Goddard, William A. A Candidate LiBH4 for Hydrogen Storage: Crystal Structures and Reaction Mechanisms of Intermediate Phases. *Appl. Phys. Lett.* **2005**, *87*, 111904.
7. Schuth, F.; Bogdanovic, B.; Felderhoff, M. Light Metal Hydrides and Complex Hydrides for Hydrogen Storage. *Chem. Commun.* **2004**, *20*, 2249–2258.
8. Vajeeston, P.; Ravindran, P.; Vidya, R.; Fjellvag, H.; Kjekshus, A. Design of Potential Hydrogen-Storage Materials Using First-Principle Density-Functional Calculations. *Crystal Growth Des* **2004**, *4–3*, 471.
9. Bogdanovic, B.; Schwickardi, M. Ti-Doped Alkali Metal Aluminum Hydrides as Potential Novel Reversible Hydrogen Storage Materials. *J. Alloys Compd.* **1997**, *1–9*, 253.
10. Blanchard, D.; Brinks, H. W.; Hauback, B. C.; Norby, P. Desorption of $LiAlH_4$ with Ti- and V-Based Additives. *Mater. Sci. Eng. B* **2004**, *108*, 54.
11. George, Lyci; Saxena, S. K. Structural Stability of Metal Hydrides, Alanates and Borohydrides of Alkali and Alkali-Earth Elements: A Review. *Int. J. Hydrogen Energy* **2010**, *35*, 5454.
12. Hauback, B. C.; Brinks, H. W.; Fjellvag, H. Accurate Structure of $LiAlD_4$ Studied by Combined Powder Neutron and X-ray Diffraction. *J. Alloys Compd.* **2002**, *346*, 184.

13. Belskii, V. K.; Bulychev, B. M.; Goluveba, A.V. *Acta Crystallogr., Sect. B: Struct. Crystallogr. Cryst. Chem.* **1982**, *38*, 1254.
14. Yoshino, M.; Komiya, K.; Takahashi, Y.; Shinzato, Y.; Yukawa, H.; Morinaga, M. Nature of the Chemical Bond in Complex Hydrides, $NaAlH_4$, $LiAlH_4$, $LiBH_4$ and $LiNH_2$. *J. Alloys Compd.* **2005**, *404*, 185.
15. Zhang, Xiao-Dong; Jiang, Zhen-Yi; Hou, Yu-Qing; Li, Li-Sha. Elastic Properties of $NaXH_4$ (X = B, Al). *J. Phys.: Condens. Matter* **2009**, *21*, 275401.
16. Vajeeston, P.; Ravindran, P.; Vidya, R.; Fjellvag, H.; Kjekshus, A. Huge-Pressure-Induced Volume Collapse in $LiAlH_4$ and its Implications to Hydrogen Storage. *Phys. Rev. B* **2003**, *68*, 212101.
17. Vajeeston, P.; Ravindran, P.; Vidya, R.; Fjellvag, H.; Kjekshus, A. Pressure-Induced Phase of NaAlH4: A Potential Candidate for Hydrogen Storage. *Appl. Phys. Lett.* **2003**, *82*, 14.
18. Hu, C. H.; Wang, Y. M.; Chen, D. M.; Xu, D. S.; Yang, K. First-Principles Calculations of Structural, Electronic, and Thermodynamic Properties of Na2BeH4. *Phys. Rev. B* **2007**, *76*, 144104.
19. Orgaz, E.; Membrillo, A.; Castaneda, R.; Aburto, A. Electronic Structure of Ternary Hydrides Based on Light Elements. *J. Alloys Compd.* **2005**, *404–406*, 176.
20. Backum, S. I.; Irodova, A. V.; Kuznetsova, S. F.; Lyakhovitskaya, O. I.; Nozik, Y. Z.; Somenkov, V. A. Crystal Structure of KGaH4. *Russ. J. Coord. Chem.* **1990**, *16*, 1210.
21. Graetz, Jason "Metastable Metal Hydrides for Hydrogen Storage". *ISRN Materials Science* **2012**, 18. ID 863025
22. Van Setten, M. J.; Popa, V. A.; De Wijs, G. A.; Brocks, G. Electronic Structure and Optical Properties of Lightweight Metal Hydrides. *Phys. Rev. B: Condens. Matter Mater. Phys.* **2007**, *75–73*, 035204.
23. Singh, D. *Planes Waves, Pseudo-Potentials and the LAPW Method*; Kluwer Academic Publishers: Boston, Dordrecht, London, 1994.
24. Schwarz, K.; Blaha, P. Solid State Calculations Using WIEN2k. *Comput. Mater. Sci.* **2003**, *28*, 259.
25. Hohenberg, P.; Kohn, W. Inhomogeneous Electron Gas. *Phys. Rev. B* **1964**, *136*, 864.
26. Kohn, W.; Sham, L. Self-Consistent Equations Including Exchange and Correlation Effects. *Phys. Rev. A* **1965**, *140*, 1133.
27. Blaha, P.; Schwartz, K.; Madsen, G. K. H.; Kvasnicka, D.; Luitz, J. "WIEN2k. An Augmented Plane Wave + Local Orbitals Program for Calculating Crystal Properties"; Techn. Universit Wien: Austria, 2001; ISBN: 3-9501031-1-2.
28. Perdew, J. P.; Burke, K.; Ernzerho, M. Generalized Gradient Approximation Made Simple. *Phys. Rev. Lett.* **1996**, 77, 3865.
29. Murnaghan, F. D. The Compressibilité of Media Under Extreme Pressures. *Prod. Natl. Acad. Sci. U.S.A.* **1944**, *30*, 244.
30. Kresse, G.; Furthmuller, J. Efficiency of Ab-Initio Total Energy Calculations for Metals and Semiconductors Using a Plane-Wave Basis Set. *Comput. Mater. Sci.* **1996**, *6*, 15.
31. Talysin, AV.; Sundqvist, B. Reversible Phase Transition in $LiAlH_4$ Under High-Pressure Conditions. *Phys. Rev. B* **2004**, *70*, 180101.
32. Chellappa, R. S.; Chandra, D.; Gramsch, S. A.; Hemley, R. J.; Lin, J. F.; Song, Y. Pressure-Induced Phase Transformations in $LiAlH_4$. *J. Phys. Chem.* **2006**, *B110*, 11088.
33. Ambrosch-Draxl, C.; Sofo, J. O. Linear optical properties of solids within the full-potential linearized augmented plane wave method. *Comput. Phys. Commun.* **2006**, *175*, 1–14.
34. Gorczyca, I.; Christensen, N. E.; Alouani, M. Calculated Optical and Structural Properties of Inp Under Pressure. *Phys. Rev. B* **1989**, *39*, 7705.
35. Kalarasse, F.; Bennecer, B.; Mellouki, A. Optical Properties of the Filled Tetrahedral Semiconductors LiMgX (X = N, P and As). *J. Phys.: Condens. Matter* **2006**, *18*, 7237.

36. Hamidani, A.; Bennecer, B. Electronic and Optical Properties of the Orthorhombic Compounds PdPX (X = S and Se). *Comput. Mater. Sci.* **2010**, *48*, 115.
37. Wooten, F. *Optical Properties of Solids*; Academic: New York, 1972.